

Experimental Full-Domain Mapping of Quantum Correlation in Clauser-Horne-Shimony-Holt Scenarios

Xin Tong^{✉,†}, Zhe He^{✉,†}, Yide Zhang^{✉,†}, Samuel Solomon[✉], Li Lin, Qiyuan Song[✉], and Lihong V. Wang^{✉,*}

Caltech Optical Imaging Laboratory, Andrew and Peggy Cherng Department of Medical Engineering, Department of Electrical Engineering, California Institute of Technology, 1200 E. California Blvd., MC 138-78, Pasadena, California 91125, USA



(Received 28 February 2022; revised 27 October 2022; accepted 14 February 2023; published 15 March 2023)

Quantum correlation between two parties serves as a useful resource in the surging applications of quantum information. The Bell nonlocality and quantum steering have been proposed to describe nonclassical correlations against local-hidden-variable and local-hidden-state theories, respectively. To characterize the two types of nonclassical correlations, various nonlocality and steering inequalities have been established, and the amount of inequality violation serves as a helpful indicator for many entanglement-based tasks. Quantum state tomography has been employed for measuring quantum states, while the method requires intensive computation and does not directly verify either nonlocality or steering over the full domain independent of established theories. Here, we experimentally map the full-domain correlation with bipartite states for nonlocality and quantum steering in Clauser-Horne-Shimony-Holt scenarios. The measurement of the maps automatically accounts for detection imperfections. Furthermore, we demonstrate the application of the correlation maps in the entanglement-based quantum key distribution protocol with arbitrary bipartite states. The correlation maps show direct measurements and simple interpretations that can answer fundamental questions about nonlocality and quantum steering as well as contribute to quantum information applications in a straightforward manner.

DOI: 10.1103/PhysRevApplied.19.034049

I. INTRODUCTION

Ever since the Einstein-Podolsky-Rosen (EPR) paradox was introduced, discussions on the EPR criterion of reality have greatly accelerated the development of quantum information theory [1–3]. Beyond the demand for applications, understanding the nature of entanglement plays an essential role in exploring the limits of classical and quantum theories [4]. The Bell-type inequalities provide a standard to test nonclassicality irrespective of quantum theories [5–10]. As the inequalities are constructed to reflect a classical prediction of local-hidden-variable (LHV) theories under a set of conditions, their violation implies the invalidity of these theories [11,12]. In 1935, Schrödinger introduced quantum steering for arbitrary measurement of bipartite entanglement [13]. Later, it was formulated using local-hidden-state (LHS) theories and applied to quantum key distribution (QKD) together with the Bell nonlocality (see Appendix A) [14–20]. For example, in the E91 QKD protocol [7], a bipartite state ρ_{AB} is shared between Alice and Bob, who perform measurements on their particles and compare their results. A

secure quantum key can be established only if the measurement results are either Bell nonlocal or quantum steerable, depending on the secure level of the devices [20–24].

The violation of the Bell-type inequalities is known as the most strict kind of quantum nonlocal condition [9,14]. In the Clauser-Horne-Shimony-Holt (CHSH) scenario where two parties (named Alice and Bob) are involved and each party has two measurement settings with two outcomes, the Bell-CHSH inequality has been widely studied [12]. In the Hilbert spaces \mathcal{A} (for Alice) and \mathcal{B} (for Bob), we denote eigenstates for the measurement axes $\hat{\alpha}$ and $\hat{\beta}$ as $A_\alpha \in \mathcal{A}$ and $B_\beta \in \mathcal{B}$ and denote the eigenvalues as a and b . The eigenvalues $a, b \in \{-1, +1\}$, where -1 and $+1$ stand for the horizontal (H) and vertical (V) polarizations. The LHV model defines a hidden variable λ with a probability density function $p(\lambda)$. For measurement outcomes a and b , their joint probability is

$$P_{\text{LHV}}(a, b|\alpha, \beta) = \int P(a|\alpha, \lambda)P(b|\beta, \lambda)p(\lambda)d\lambda, \quad (1)$$

where $P(a|\alpha, \lambda)$ and $P(b|\beta, \lambda)$ are the probabilities for Alice to obtain a and Bob to obtain b , respectively. For a chosen pair of α and β , $E(\alpha, \beta)$ is defined as the correlation

*lvw@caltech.edu

†These authors contributed equally.

of the measurement [25]:

$$\begin{aligned} E(\alpha, \beta) &\equiv P(H, H|\alpha, \beta) + P(V, V|\alpha, \beta) \\ &\quad - P(H, V|\alpha, \beta) - P(V, H|\alpha, \beta). \end{aligned} \quad (2)$$

The Bell-CHSH inequality is given by [12,26]

$$S_{\text{CHSH}} = |E(\alpha, \beta) + E(\alpha', \beta) - E(\alpha, \beta') + E(\alpha', \beta')| \leq 2, \quad (3)$$

where α' and β' denote the second chosen pair of the analyzer angles. This inequality serves as an experimentally efficient benchmark for Bell's test [27]. Previous experiments have proven the violation of the Bell-CHSH inequality with entangled photons [28–30]. Other than testing against LHV models, the S_{CHSH} value itself is of great significance. Studies have shown that the S_{CHSH} values are closely linked to the fidelity of quantum teleportation [31,32], the certification of random number generation [33], the investigation of entanglement distillability [34,35], and the security level of a certain QKD protocol [36–39].

Quantum steering [Fig. 1(a) and Appendix A] involves a similar violation of the LHS model [14,40,41], where Eq. (1) reduces to

$$P(a, b|\alpha, \beta) = \int P(a|\alpha, \lambda) \text{Tr}(\Pi_{b|\beta} \rho_\lambda) p(\lambda) d\lambda. \quad (4)$$

Here, $\Pi_{b|\beta}$ is the detection projector ($\Pi_{b|\beta} = |b\rangle_\beta \langle b|_\beta$), and ρ_λ is the local hidden state related to λ . The LHS model hypothesizes that Bob receives ρ_λ . If Bob's measurements are mutually unbiased (i.e., $|\langle \beta' | \beta \rangle|^2 = 1/2$), the analogous inequality as an unsteerable condition is given by [25,42]

$$\begin{aligned} S_{\text{QS}} &= \sqrt{[E(\alpha, \beta) + E(\alpha', \beta)]^2 + [E(\alpha, \beta') + E(\alpha', \beta')]^2} \\ &\quad + \sqrt{[E(\alpha, \beta) - E(\alpha', \beta)]^2 + [E(\alpha, \beta') - E(\alpha', \beta')]^2} \\ &\leq 2. \end{aligned} \quad (5)$$

From $|\langle \beta' | \beta \rangle|^2 = 1/2$, we have $\Delta\beta \triangleq \beta' - \beta = 45^\circ$ [25]. The same setting also applies to S_{CHSH} [29,43–45]. Hence, the angle set becomes $(\alpha, \alpha', \beta, \beta') \rightarrow (\alpha, \alpha', \beta, \beta + 45^\circ)$.

The S values in inequalities (3) and (5) provide straightforward criteria to characterize nonlocality and steering and serve as useful indicators for various quantum information tasks [4,9,20]. Statistically significant violations of the inequalities have been predicted and experimentally observed with maximally entangled states. However, practical imperfections almost always exist, deviating the experimental states from the ideal ones. Quantum state tomography (QST) has been widely utilized to reconstruct the density matrix of the experimental state [46,47].

Nevertheless, the reconstruction in QST depends on the measurement apparatus and settings, and can be computationally expensive and prone to experimental errors [48–52]. Tremendous efforts have been devoted to efficiently and accurately reconstructing the states in the presence of measurement errors [53–56]. Moreover, the dependence of QST on quantum theories to test against classical such as LHV models may suffer from circular reasoning. For these reasons, direct experimental evidence is essential for the clarification of nonlocality and steering.

Here, rather than obtaining a complete description of the states, we experimentally measure the S values by sampling all possible observation angles with a step size; the resultant full-domain S maps are less vulnerable to detection errors. The regions where $S_{\text{CHSH}} > 2$ and $S_{\text{QS}} > 2$ indicate violation of LHV and LHS, respectively. The measured S maps are shown to be consistent with those reconstructed through QST. Moreover, S maps can be applied to arbitrary bipartite sources, including partially entangled states. As an application, we use S maps to calibrate the E91 QKD protocol and optimize measurement setting selections. The simple and direct measurement of S values may benefit various entanglement-related tasks.

II. RESULTS

A. Experimental setup

The experimental setup designed in this work is shown in Fig. 1 [57,58]. A 50-mW continuous-wave laser operating at 405-nm wavelength provides the pump beam. A spontaneous parametric down-conversion (SPDC) β -barium borate (BBO) crystal is used to generate polarization-entangled bipartite Bell states [59]. The pump beam propagates through a linear polarizer, a half-wave plate (HWP), a variable wave plate, and a quartz plate before reaching the BBO crystals, where a fraction of the photons spontaneously decay into photon pairs with a wavelength twice that of the pump [60]. The propagation directions of the photon pairs form a cone symmetrically around the pump beam because $\vec{k}_s + \vec{k}_i = \vec{k}_p$, where the subscripts s , i , and p of the wavevectors denote the signal, idler, and pump, respectively [61]. The signal and idler photons propagate approximately 1 m in free space to ensure sufficient spatial separation. Next, a pair of HWPs followed by polarizing beam splitters (PBSs) set angles α and β to measure the polarizations of the signal and idler photons, respectively. Finally, after passing through bandpass filters to reject ambient light, the photons are received through lenses by two single-photon counting modules (SPCMs). The two SPCMs are connected to a field-programmable gate-array-based time controller, enabling coincidence counting. By automatically motorizing the HWPs, we scan (α, β) and record the coincidence count $N(H, H|\alpha, \beta)$ within one second per set, thus forming a full-domain map of coincidences over all possible

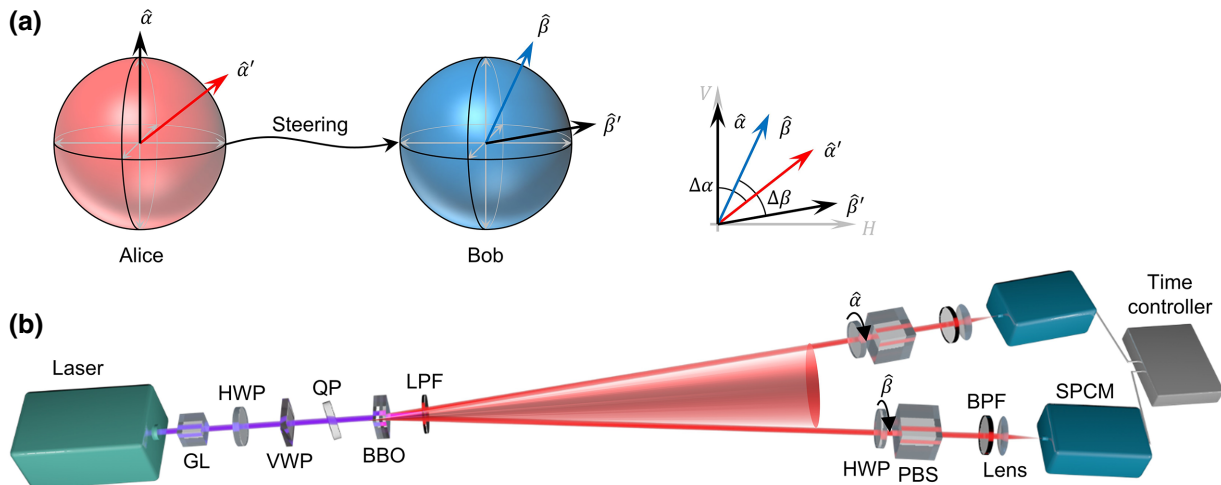


FIG. 1. Schematics of quantum steering concept and full-domain mapping setup. (a) Schematic illustration of quantum steering. Two observers, Alice and Bob, measure the polarizations of signal and idler photons at angles α , α' , β , and β' in their respective subsystems. The link in between shows quantum steering from Alice to Bob. (b) Experimental setup for coincidence measurement. The Glan-Laser polarizer (GL) and half-wave plate (HWP) adjust the polarization angle θ_p of the pump laser. A variable wave plate (VWP) and a quartz plate (QP) adjust the relative phase ϕ_d . A pair of type-I β -barium borate (BBO) crystals generate the entangled states via the process of spontaneous parametric down-conversion (SPDC). Two HWPs behind the SPDC are motorized for automatic scanning. Each HWP, together with the subsequent polarizing beam splitter (PBS), sets the corresponding observation angle of polarization, α or β . A bandpass filter and a lens are mounted before each SPCM to reject the ambient light and focus the SPDC photons onto the detector. The coincidences of the two SPCMs are measured by a time controller and used for Bell's test and S maps.

angle sets for a given step size. More details of the setup can be found in Appendix B.

The pump photons, through polarization elements, are set to the following superposition state:

$$|\psi_p\rangle = \cos \theta_p |V\rangle_p + \exp(i\phi_p) \sin \theta_p |H\rangle_p, \quad (6)$$

where $|V\rangle$ and $|H\rangle$ denote the vertical and horizontal polarization states. $\cos \theta_p$ and $\sin \theta_p$ are the amplitudes, and ϕ_p is the relative phase. The wave function of the SPDC photon pairs (termed “signal” and “idler” photons) is given by

$$|\psi_{\text{SPDC}}\rangle = \cos \theta_p |H\rangle_s |H\rangle_i + \exp(i\phi_d) \sin \theta_p |V\rangle_s |V\rangle_i, \quad (7)$$

where ϕ_d is the relative phase averaged over the distributions in both propagation direction and frequency of all the photon pairs, and the subscripts s and i denote signal and idler, respectively [26]. When $\theta_p = 45^\circ$ and $\phi_d = 0^\circ$, the photon pairs are in a maximally entangled Bell state (namely, an EPR state),

$$|\psi_{\text{EPR}}\rangle = \frac{1}{\sqrt{2}} (|H\rangle_s |H\rangle_i + |V\rangle_s |V\rangle_i). \quad (8)$$

Values of (θ_p, ϕ_d) other than $(45^\circ, 0^\circ)$ and $(45^\circ, 90^\circ)$ lead to unbalanced bipartite states. Additionally, the purity of the entangled photon pairs is almost always contaminated by practical imperfections (e.g., stray light), leading to mixed states.

B. Violation of the Bell-CHSH inequality and full-domain coincidence measurement

The Bell-CHSH inequality provides a benchmark for nonlocality distinction. LHV theories show that $S_{\text{CHSH}} \leq 2$ [Eq. (3)]; however, quantum theories predict that $S_{\text{CHSH}} > 2$ is possible at specific observation angles. The EPR state exhibits the maximum violation at $(\alpha = 0^\circ, \beta = 22.5^\circ, \alpha' = 45^\circ, \beta' = 67.5^\circ)$ at Tsirelson's bound, $S_{\text{CHSH}}^{\max} = 2\sqrt{2}$ [62].

We prepare an experimental EPR state and estimate the density matrix using QST, as shown in Figs. 2(a) and 2(b). The reconstruction is based on a fast maximum-likelihood estimation (MLE) algorithm with 36 projective measurements [63]. According to the estimated density matrix $\hat{\rho}_{\text{EPR}}$, we calculate the fidelity and concurrence to characterize the state [64,65]. Bell's test is performed at $(\alpha = 0^\circ, \beta = 22.5^\circ, \alpha' = 45^\circ, \beta' = 67.5^\circ)$ and their orthogonal counterparts, which maximize S_{CHSH} to

$$S_{\text{CHSH}} = 2.692 \pm 0.007. \quad (9)$$

To better visualize the coincidence counts as a function of α and β , we vary α to $0^\circ, 45^\circ, 90^\circ$, and 135° and detect coincidences over nine β angles for each α , as shown in Fig. 2(c). More details can be found in Note S1 within the Supplemental Material [66] and Appendix B.

Next, we measure the full-domain coincidence map (referred to as N map). We repeat the finer-grid scan of the coincidence count $N(H, H|\alpha, \beta)$ ten times with a step

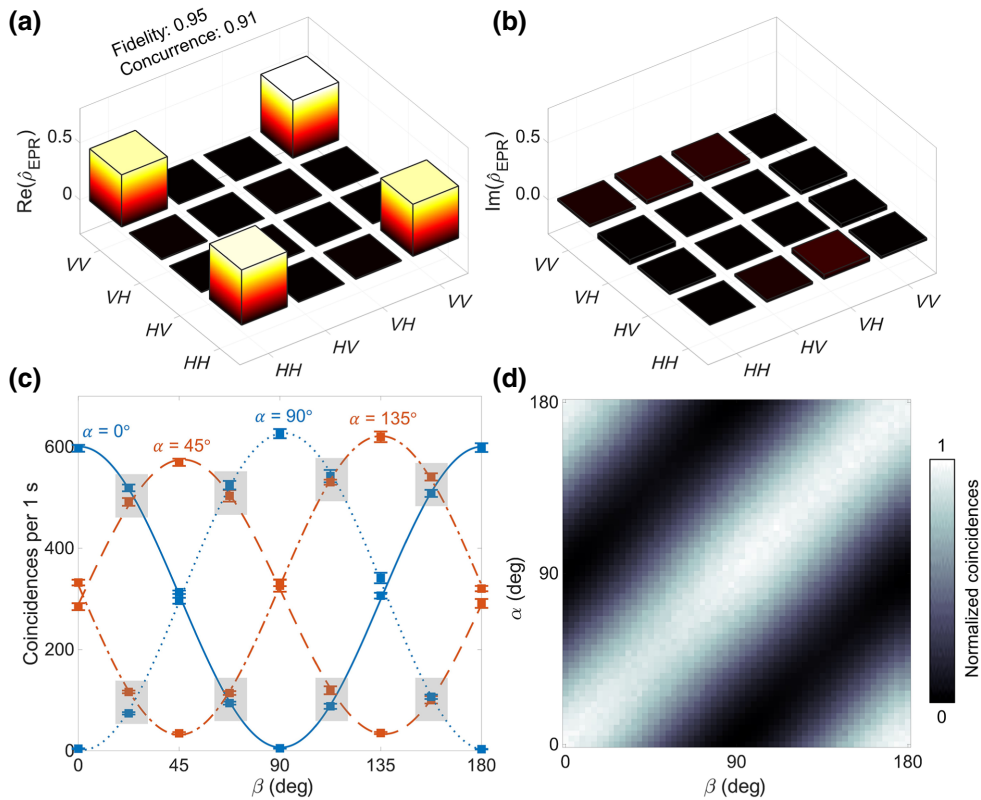


FIG. 2. Characterization of the experimental EPR state. Real (a) and imaginary (b) parts of the density matrix of the experimental EPR state, reconstructed from QST. The fidelity and concurrence of the state are calculated accordingly. (c) Coincidences as a function of β when $\alpha = 0^\circ, 45^\circ, 90^\circ, 135^\circ, 180^\circ$. Experimental results are plotted as means \pm standard errors of the means ($n=9$). The curves are fitted based on Eq. (S2) in Note S1 within the Supplemental Material [66]. The data points marked by gray rectangles are used to calculate the S_{CHSH} value. (d) Measurements of the full-domain coincidence map $N(H, H|\alpha, \beta)$ with 61×61 points.

size of 3° and the averaged result is presented in Fig. 2(d). A detailed description of the map, including the statistical errors, is shown in Fig. S1 within the Supplemental Material [66]. Note that Bell's test requires only a subset of the map and gives only a single S_{CHSH} value for maximum violation. The full-domain coincidence map renders a superset of the conventional sparse-angle Bell's test.

C. Mapping nonlocality and quantum steering

Three steps are required to construct the S map from a full-domain N map, as shown in Fig. 3. In the first step [Fig. 3(a)], the original $N(H, H|\alpha, \beta)$ map is shifted to form three additional maps [i.e., $N(H, H|\alpha + 90^\circ, \beta)$, $N(H, H|\alpha, \beta + 90^\circ)$, and $N(H, H|\alpha + 90^\circ, \beta + 90^\circ)$], which are assumed to be equivalent to $N(V, H|\alpha, \beta)$, $N(H, V|\alpha, \beta)$, and $N(V, V|\alpha, \beta)$, respectively. In the second step [Fig. 3(b)], the four N maps are combined into a full-domain correlation map [referred to as an E map according to Eq. (2)] using Eq. (B1). Four points on the E map represent two separate measurements by Alice and Bob at polarization angles $(\alpha, \alpha', \beta, \beta')$ (see Fig. S2 within the Supplemental Material [66]). The E map can be used

to describe observations made by the two observers with arbitrary choices of $(\alpha, \alpha', \beta, \beta')$.

In the last step, two protocols are used to describe the entanglement from the E map. Calculation over $(\alpha, \alpha', \beta, \beta')$ using Eq. (3) from 0° to 180° yields a four-dimensional (4D) S_{CHSH} map. The Bell-CHSH inequality demarcates the 4D nonlocality region. Specifically, by examining the hyperplane where $\beta' - \beta = 45^\circ$, the three-dimensional (3D) $S_{\text{CHSH}}(\alpha, \alpha', \beta, \beta + 45^\circ)$ map renders choices for Bob to achieve nonlocal observations, as shown in Fig. 3(c). In contrast, quantum steering poses a weaker violation condition, as shown in Eq. (5). Similar to the S_{CHSH} calculation, we convert the E map to the 3D S_{QS} map, as shown in Fig. 3(d). Because S values are based on independent measurements, we exclude the hyperplanes where $\alpha' = \alpha$ and $\alpha' = \alpha \pm 90^\circ$, as shown in Figs. 3(c) and 3(d) as dashed lines. For simplicity, we omit the dashed lines in all the following figures.

Following the procedure above, we experimentally measure the S_{CHSH} and S_{QS} maps for the EPR state, as shown in Fig. 4. In the $(\alpha, \alpha', \beta, \beta + 45^\circ)$ hyperplane, α , α' , and β are all arbitrarily chosen. The S_{CHSH} map [Figs. 4(a) and 4(b)] demarcates the regions where the

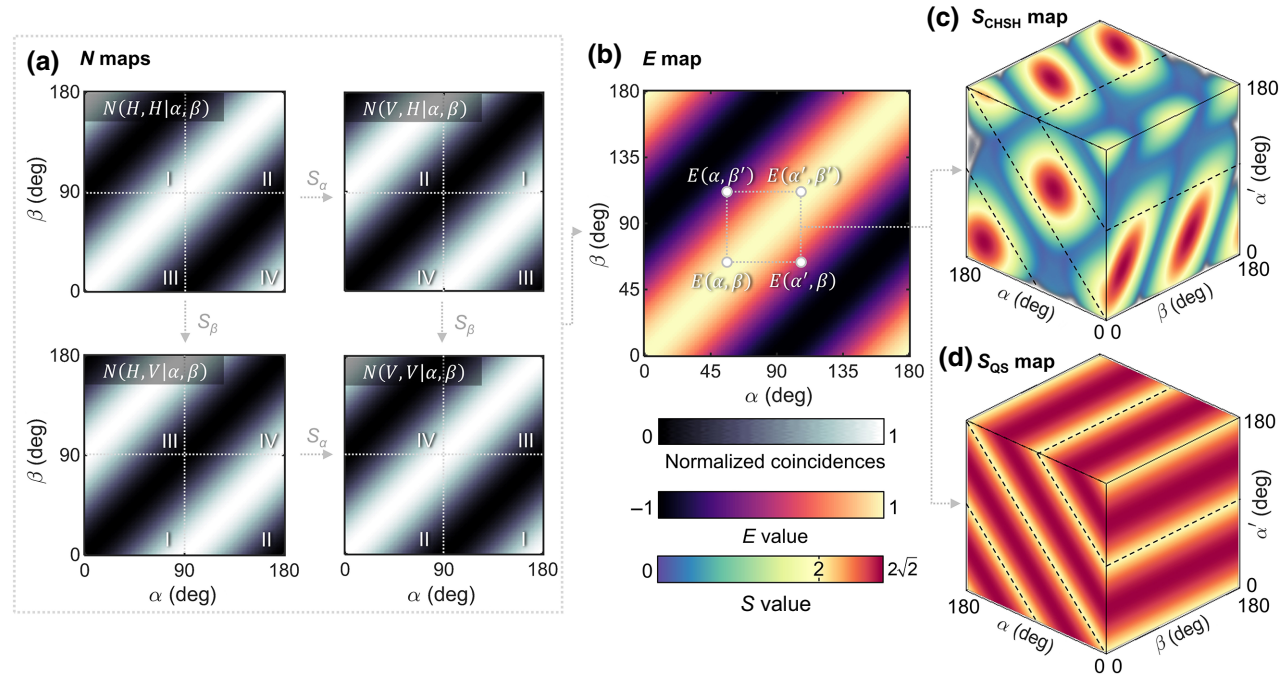


FIG. 3. Illustration of the S-map calculation through simulation. (a) Simulated full-domain coincidence (N) maps. The $N(H,H)$ map is shifted by 90° along the α axis (denoted as S_α) to obtain the $N(V,H)$ map and by 90° along the β axis (denoted as S_β) to obtain the $N(V,H)$ map. Similarly, either $N(V,H)$ or $N(H,V)$ map can be shifted to obtain the $N(V,V)$ map. (b) Simulated full-domain correlation (E) map based on the basic operations of the four shifted N maps. Four points on the map are selected for S value calculation. (c) Simulated full-domain 3D Bell-CHSH map $S_{\text{CHSH}}(\alpha, \alpha', \beta, \beta' = \beta + 45^\circ)$, acquired from the E map using Eq. (3). Dashed lines denote the hyperplanes to be excluded, where $\alpha' = \alpha$ and $\alpha' = \alpha \pm 90^\circ$. (d) Simulated full-domain 3D quantum steering map $S_{\text{QS}}(\alpha, \alpha', \beta, \beta' = \beta + 45^\circ)$, acquired from the E map using Eq. (5). Dashed lines denote the hyperplanes to be excluded, where $\alpha' = \alpha$ and $\alpha' = \alpha \pm 90^\circ$.

Bell-CHSH inequality is violated. We also compute the two-dimensional (2D) S_{CHSH} map [Fig. 4(c)] using the QST-reconstructed density matrix, which is consistent with Fig. 4(b). Similarly, on the experimentally measured S_{QS} map [Figs. 4(d) and 4(e)], an angle combination achieving $S_{\text{QS}} > 2$ provides a violation of the LHS theory. The QST-reconstructed 2D S_{QS} map is shown in Fig. 4(f) for comparison.

We propose to define the LHV and LHS violation ratios, respectively, as

$$\eta_{\text{CHSH}} \equiv \frac{\mathcal{V}\{S_{\text{CHSH}} > 2\}}{\mathcal{V}\{\text{All}\}}, \eta_{\text{QS}} \equiv \frac{\mathcal{V}\{S_{\text{QS}} > 2\}}{\mathcal{V}\{\text{All}\}}, \quad (10)$$

where \mathcal{V} denotes the volume of the part of the domain under the specified condition. For the experiment using the EPR state, the measured values of $\eta_{\text{CHSH}} = 0.17$ and $\eta_{\text{QS}} = 0.93$ agree with the theoretical values [see Figs. S4(a) and S4(b) within the Supplemental Material [66]].

D. Correlation maps with different unbalanced bipartite states

Thus far, we focus on the EPR state, but few systems can yield a perfect balance between $|H\rangle|H\rangle$ and $|V\rangle|V\rangle$ states.

For example, with states described by Eq. (7), S maps generally rely on θ_p (pump polarization) and ϕ_d (relative phase). By adjusting the HWP, variable wave plate, and quartz plate before the BBO crystals, we tune the SPDC states with representative θ_p and ϕ_d values. The experimental $N(H,H)$ maps and the associated S_{CHSH} and S_{QS} maps are summarized in Figs. 5(a)–5(i) and Fig. S2 within the Supplemental Material [66].

Another example is given by the Werner states, whose density matrices can be described by [11]

$$\rho_W = p |\psi_{\text{EPR}}\rangle \langle \psi_{\text{EPR}}| + (1-p) \frac{I}{4}, \quad (11)$$

where $I/4$ denotes the maximally mixed state, and p is the weight of the pure state. By adding a light-emitting diode and varying its intensity, we tune the Werner states with different p values. As an example, for $p \approx 0.25$, the coincidence maps and the associated S_{CHSH} and S_{QS} maps are summarized in Figs. 5(j)–5(l).

For all the states defined in Eqs. (7) and (11), the corresponding calculations of the $N(H,H)$ and S maps based on QST can be found in Figs. S3 and S4 within the Supplemental Material [66], which agree with our experimental observations.

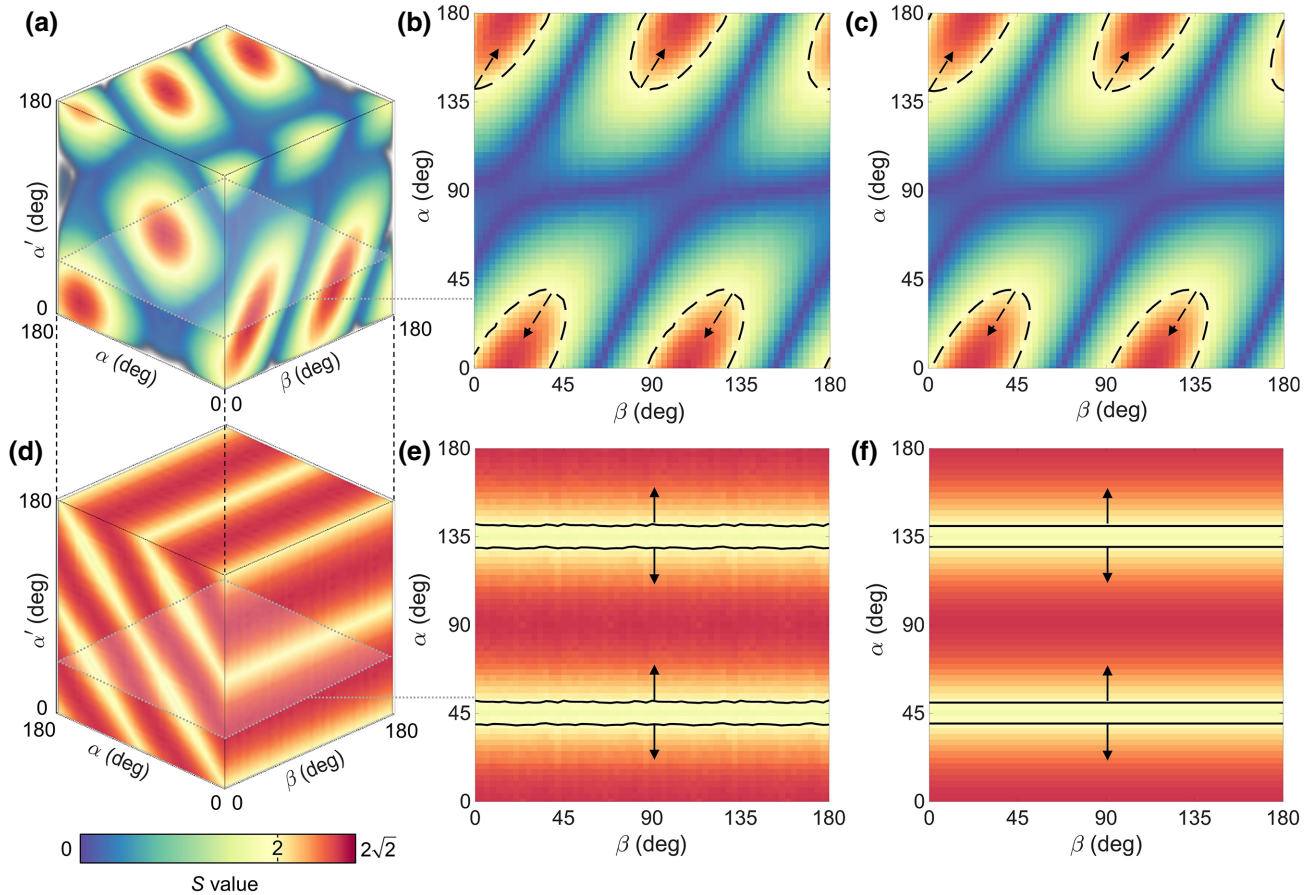


FIG. 4. Experimental full-domain S_{CHSH} and S_{QS} maps. (a) 3D experimentally measured $S_{\text{CHSH}}(\alpha, \alpha', \beta, \beta' = \beta + 45^\circ)$ map. (b) 2D experimentally measured cross-section map of $S_{\text{CHSH}}(\alpha, \alpha' = 45^\circ, \beta, \beta' = \beta + 45^\circ)$, corresponding to the region enclosed by the gray dotted line in (a). The interiors of the dashed contours indicated by the dashed arrows show the region where $S_{\text{CHSH}} > 2$. (c) 2D QST-reconstructed cross-section map of $S_{\text{CHSH}}(\alpha, \alpha' = 45^\circ, \beta, \beta' = \beta + 45^\circ)$. (d) 3D experimentally measured $S_{\text{QS}}(\alpha, \alpha', \beta, \beta' = \beta + 45^\circ)$ map. (e) 2D experimentally measured cross-section map of $S_{\text{QS}}(\alpha, \alpha' = 45^\circ, \beta, \beta' = \beta + 45^\circ)$, corresponding to the region enclosed by the gray dotted line in (d). The interiors of the solid contours indicated by the solid arrows show the region where $S_{\text{QS}} > 2$. (f) 2D QST-reconstructed cross-section map of $S_{\text{QS}}(\alpha, \alpha' = 45^\circ, \beta, \beta' = \beta + 45^\circ)$.

E. Calibrated quantum key distribution protocol based on correlation maps

From direct measurements, the S maps enable versatile applications in quantum information, illustrated here on the basis of the E91 QKD protocol [7]. In the typical E91 protocol, entangled states are shared between Alice and Bob, who then distribute a secret key against an eavesdropper, Eve. Prior to their measurements, Alice and Bob decide on their respective polarization angle sets $\{\alpha_1, \alpha_2, \alpha_3\}$ and $\{\beta_1, \beta_2, \beta_3\}$, from which they can arbitrarily select and measure. Here, $\alpha_1, \alpha_3, \beta_1, \beta_3$ are four different angles, α_2 takes value from β_1 or β_3 , and β_2 takes value from α_1 or α_3 . After measurements, they compare their series of angle choices. The measurement results with different angles are shared to calculate the S_{CHSH} or S_{QS} values and thus evaluate the security of QKD. The results measured with the same angles are kept private and converted into the secret key if security is confirmed. In

the original E91 protocol using an EPR state, the corresponding angles for Alice and Bob are $\{0^\circ, 22.5^\circ, 45^\circ\}$ and $\{22.5^\circ, 45^\circ, 67.5^\circ\}$.

Due to imperfections in entanglement sources and experimental settings, the angle sets proposed above are not always optimal. For some non-EPR states, it has been shown that different measurement settings can maximize Bell's inequality violation [67]. By measuring the S maps of the setup prior to communication, we can calibrate the measurement settings and optimize the angle sets $\{\alpha_1, \alpha_2, \alpha_3\}$ and $\{\beta_1, \beta_2, \beta_3\}$ not only for an EPR state but also for arbitrary bipartite states, thus generalizing the E91 protocol, as shown in Fig. 6. In the two-way scenario where both Alice's and Bob's devices are prone to eavesdropping, the optimal choices for $\{\alpha_1, \alpha_3, \beta_1, \beta_3\}$ are given by the point that maximizes the S_{CHSH} value in the four-dimensional S_{CHSH} map, as shown in Figs. 6(a)–(c). α_2 (β_2) is then chosen to be equal to β_1 (α_1) or β_3 (α_3),

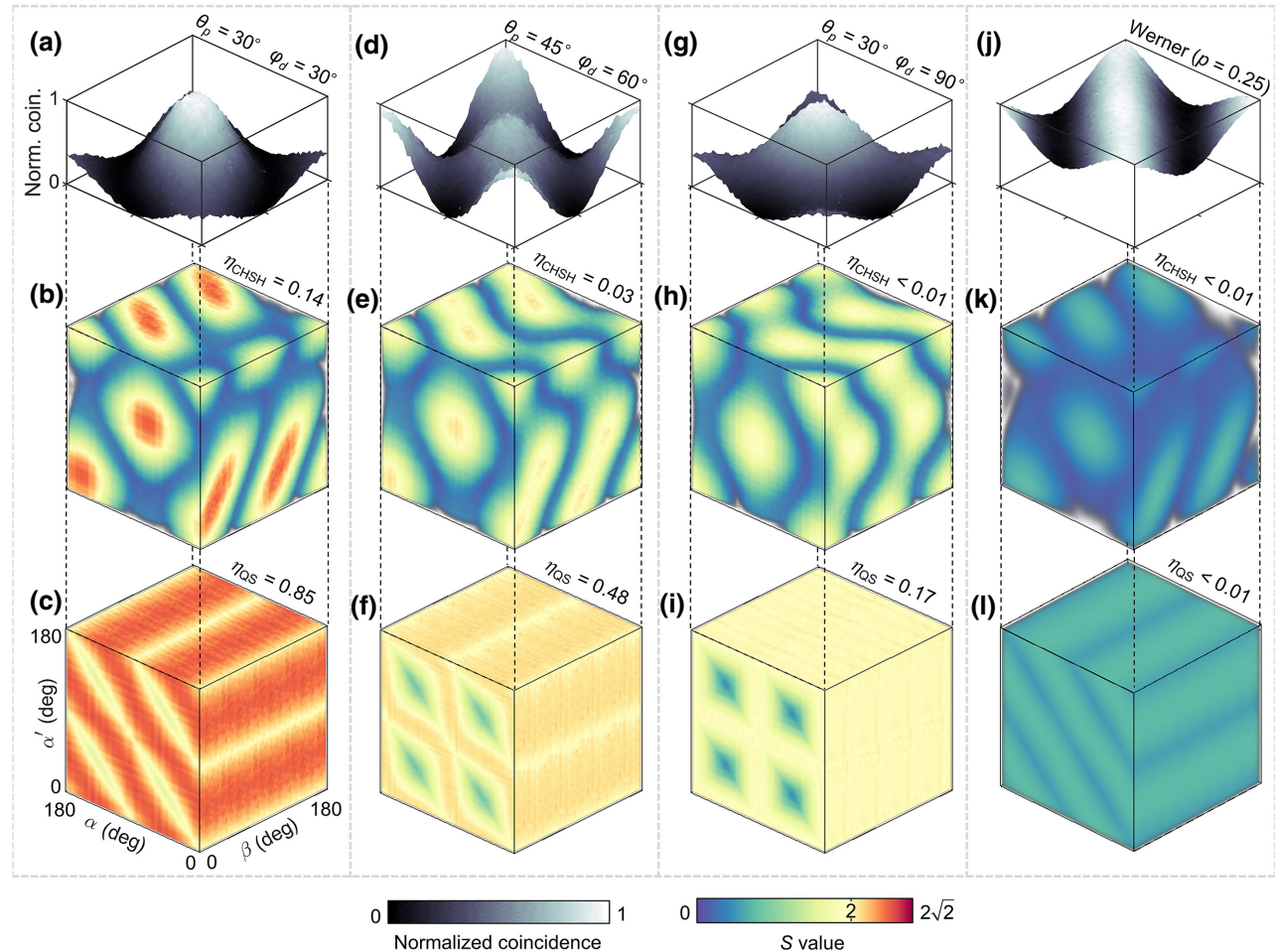


FIG. 5. Experimental full-domain $N(H, H)$ and S maps with unbalanced bipartite states and Werner states. Experimental $N(H, H)$ map (a), 3D S_{CHSH} map (b), and 3D S_{QS} map (c) of unbalanced bipartite states with $\theta_p = 30^\circ, \phi_d = 30^\circ$. Norm. coin., normalized coincidences per 1 s. Experimental $N(H, H)$ map (d), 3D S_{CHSH} map (e), and 3D S_{QS} map (f) of unbalanced bipartite states with $\theta_p = 45^\circ, \phi_d = 60^\circ$. Experimental $N(H, H)$ map (g), 3D S_{CHSH} map (h), and 3D S_{QS} map (i) of unbalanced bipartite states with $\theta_p = 30^\circ, \phi_d = 90^\circ$. Experimental $N(H, H)$ map (j), 3D S_{CHSH} map (k), and 3D S_{QS} map (l) of Werner states with $p = 0.25$.

whichever maximizes the coincidences, as shown in the diagonal line in Fig. 6(d). For the EPR state, the protocol above recovers the angle sets in the original E91 proposal. When the experimental states deviate from the perfect EPR state, however, the optimal measurement settings might differ from $\{0^\circ, 22.5^\circ, 45^\circ\}$ and $\{22.5^\circ, 45^\circ, 67.5^\circ\}$ and can be located through S maps, as shown in Fig. 6 and Figs. S5 and S6 within the Supplemental Material [66].

Other than the optimal measurement settings, S maps also render a broader choice space for secure QKD under more general attacks from Eve, such as the collective attack [22,36]. When the measurement settings deviate from the optimal ones but remain within the LHV or LHS violation regions, the S values would be lower. Moreover, suboptimal measurement settings can also lead to lower coincidence counts and higher qubit error rates [68]. Nevertheless, with error correction and privacy amplification,

secure QKD remains possible when the key rate is positive [69]. Under the assumptions of perfect detector efficiency and asymptotically infinite key length, we calculate the key rates under collective attack (denoted as the r map) in the device-independent scenario [22,70]. The r maps [Fig. 6(e)] demarcate the positive key rate region, which can be combined with the S maps to render all the feasible choices for Alice and Bob [Fig. 6(g)]. Similar to the violation ratios η_{CHSH} and η_{QS} , one can define the positive key ratio η_r :

$$\eta_r = \frac{\mathcal{V}\{r > 0\}}{\mathcal{V}\{\text{All}\}}, \quad (12)$$

which can serve as an indicator of the security level of the experimental states. For the experimental EPR state, $\eta_r = 0.035$, as shown in Fig. 6(f).

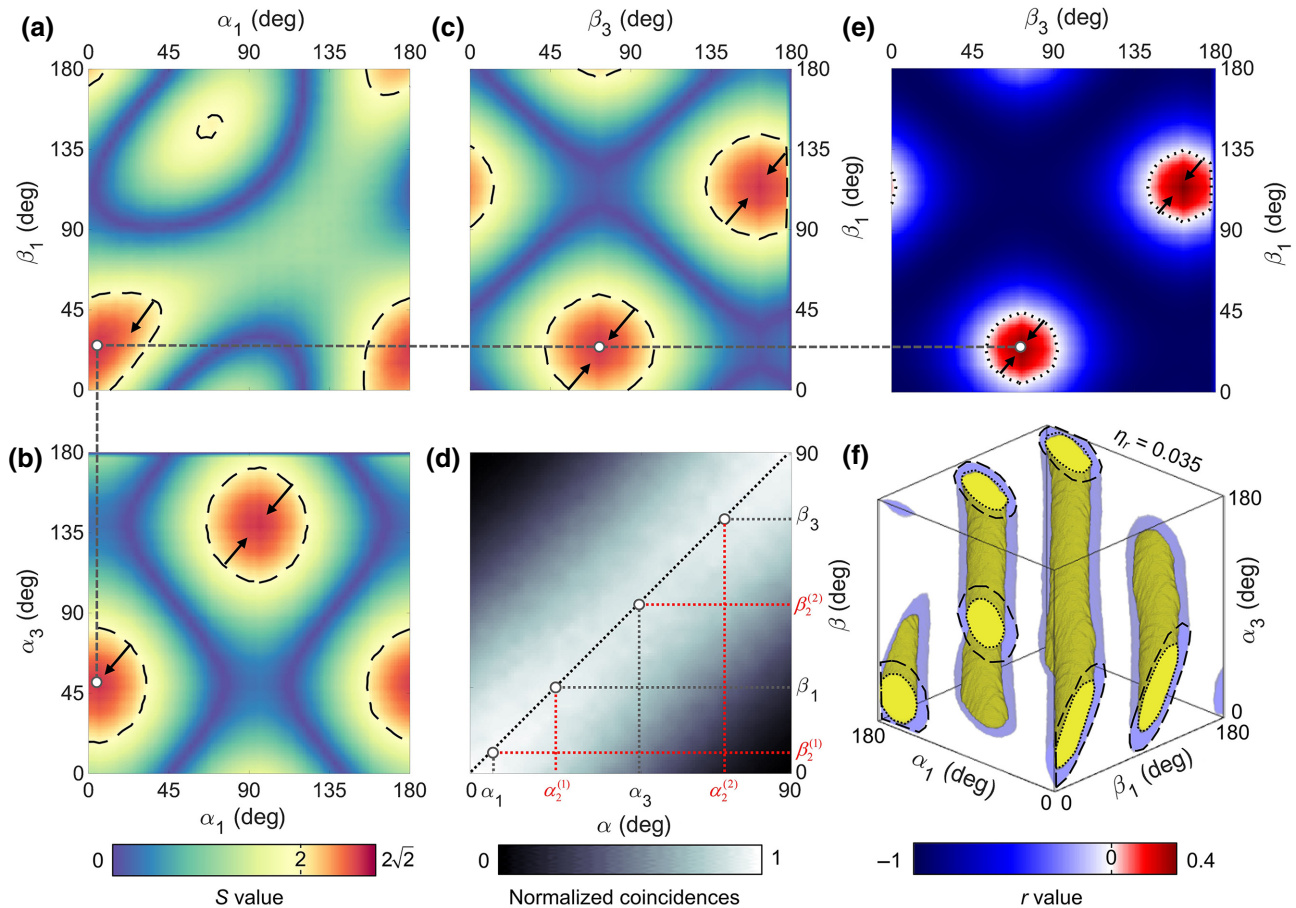


FIG. 6. Correlation maps with the experimental EPR state for the calibrated E91 protocol. 2D experimental S_{CHSH} maps for $\{\alpha_1, \beta_1; \alpha_3 = 48^\circ, \beta_3 = 72^\circ\}$ (a), $\{\alpha_1, \alpha_3; \beta_1 = 24^\circ, \beta_3 = 72^\circ\}$ (b), and $\{\beta_1, \beta_3; \alpha_1 = 6^\circ, \alpha_3 = 48^\circ\}$ (c) showing the region (indicated by black dashed contours and arrows) enabling key distribution. Gray-white circles mark the optimal angle set for maximal Bell-CHSH inequality violation. Gray dashed lines connect the same angle set in different hyperplanes. (d) Experimental coincidence map presenting the optimal choices for α_2 and β_2 (marked by red dotted lines), to be selected within $\{\beta_1, \beta_3\}$ and $\{\alpha_1, \alpha_3\}$ (marked by gray dotted lines), respectively. Black dotted line represents the diagonal that maximizes coincidences. (e) 2D experimental r map for $\{\beta_1, \beta_3; \alpha_1 = 6^\circ, \alpha_3 = 48^\circ\}$ showing the region (indicated by black dotted contours and arrows) with positive key rates under collective attack. (f) 3D experimental masks for $\{\alpha_1, \alpha_3, \beta_1, \beta_3 = \beta_1 + 45^\circ\}$ showing the CHSH violation region and the positive key-rate region.

III. DISCUSSION

The S maps proposed in this study enable direct full-domain tests against the LHV and LHS theories with arbitrary bipartite states in CHSH scenarios. The full S map in 4D space grants versatility to analyze any hyperplane. For instance, to exhibit a steerable state, different analyzer sets ($\beta, \beta + 45^\circ$) should be adopted by Bob to check whether $S_{\text{QS}} > 2$. In the S maps, $S_{\text{CHSH}} > 2$ proves to be a sufficient condition for $S_{\text{QS}} > 2$, and the fact that $\eta_{\text{CHSH}} < \eta_{\text{QS}}$ agrees with the widely studied hierarchy of quantum entanglement [14,71,72]. The maps render two regions for Bob's measurements: the steering region $\{(\alpha, \alpha', \beta) : S_{\text{QS}}(\alpha, \alpha', \beta, \beta + 45^\circ) > 2\}$ and the Bell nonlocal region $\{(\alpha, \alpha', \beta) : S_{\text{CHSH}}(\alpha, \alpha', \beta, \beta + 45^\circ) > 2\}$. These regions help Bob answer the fundamental question of whether his measurement is nonlocal or steerable, which evaluates the

security of the measurement. For example, the independence of the contours on β in Figs. 4(e) and 4(f) clearly illustrate that Bob's choice of β cannot affect S_{QS} , while Alice's choices of (α, α') can vary S_{QS} . This phenomenon reflects the fact that the joint measurement is steerable from Alice to Bob but not necessarily steerable in the opposite direction.

The LHV and LHS violation ratios (i.e., η_{CHSH} and η_{QS}) defined in Eq. (10) represent the proportion of the $S > 2$ regions over the whole S maps. For pure states described by Eq. (7), Fig. S7 within the Supplemental Material presents the range of η_{CHSH} and η_{QS} [66]. For product states, $\eta_{\text{CHSH}}^{\min} = \eta_{\text{QS}}^{\min} = 0$. For the maximally entangled state (i.e., the EPR state), $\eta_{\text{CHSH}}^{\max} \approx 0.2$, $\eta_{\text{QS}}^{\max} = 1$. Our experimental EPR states show lower S and η values than their upper bounds mostly due to the nonzero ϕ_d value. Since ϕ_d is the relative phase averaged over all the

photon pairs, it is difficult to be fully compensated by the VWP and QP. Using Eq. (S2), we estimate the experimental value of $\phi_d \approx 27^\circ$. Accordingly, simulated η values shown in Figs. S4(a) and S4(b) within the Supplemental Material agree well with the experimental values [66]. Compared to existing metrics such as entropy, fidelity, and concurrence, the violation ratio is straightforward without the knowledge of the density matrix [64,65,73].

Based on direct measurements, the correlation maps present a straightforward interpretation of the quantum correlation. To test against classical such as LHV models, fewer underlying assumptions are preferred to avoid logical flaws. Although one can perform QST to construct the density matrix of the state and predict its projective measurement results, the calculation depends on the quantum theories. Therefore, using such S values for Bell's tests will suffer from circular reasoning. There are various ways to acquire the S maps, depending on the complexity of underlying assumptions. The first method is to directly scan over the full domain and measure the S maps experimentally. Since such S values do not depend on quantum mechanical theories, this method is suitable for characterizing the nonlocality and steering. With fewer measurements, QST can faithfully reconstruct the S maps. However, the data analysis in QST can be computationally intensive [50], and the optimal measurement settings depend on the states to be measured [74]. Finally, in some rare cases where more prior information of the state is known, the S maps may be explicitly derived or calculated. For example, for unbalanced states described by Eq. (7), the variations of θ_p and ϕ_d have distinct effects on S maps (see Fig. S4 within the Supplemental Material [66]). In the extreme case, if the relative phase between the $|H\rangle|H\rangle$ and $|V\rangle|V\rangle$ states approaches 90° , Eq. (S2) in Note S1 within the Supplemental Material becomes [66]

$$\begin{aligned} P(H,H|\alpha,\beta;\theta_p,\phi_d=90^\circ) &= (\sin \alpha \sin \beta \cos \theta_p)^2 \\ &+ (\cos \alpha \cos \beta \sin \theta_p)^2. \end{aligned} \quad (13)$$

When θ_p reaches 0° or 90° , either $|H\rangle|H\rangle$ or $|V\rangle|V\rangle$ dominates, yielding

$$\begin{aligned} P(H,H|\alpha,\beta;\theta_p=0^\circ,\phi_d) &= (\sin \alpha \sin \beta)^2, \\ P(H,H|\alpha,\beta;\theta_p=90^\circ,\phi_d) &= (\cos \alpha \cos \beta)^2. \end{aligned} \quad (14)$$

As shown in Fig. 5(i), these states are mostly local since $\eta_{\text{CHSH}} < 0.01$. This case is calculated in detail in Appendix A. After correcting for the detection errors, the S maps obtained by all three methods are consistent.

Other than theoretical and computational simplicity, direct measurement of S maps also complements QST by considering experimental imperfections. QST can be used to find the maximum S value, but systematic errors in the detection apparatus can affect the accuracy of QST reconstruction, thus biasing the S -value measurement

[52,75]. For example, misalignment errors in the HWPs can deviate the optimal measurement settings from the original ones shown in Fig. 2(c), as demonstrated in Figs. S8(d)–S8(f) within the Supplemental Material [66]. Moreover, QWP misalignment might reduce the maximum S values, as shown in Figs. S8(g)–S8(i) within the Supplemental Material [66]. Similarly, polarization-dependent inefficiencies in the detectors or analyzers can also decrease S values, as shown in Figs. S8(j)–S8(l) within the Supplemental Material [66]. All the examples can deviate the measurement basis from the mutually unbiased ones. Accordingly, the QST-reconstructed S maps can differ from the experimental ones, thus hindering accurate understanding and appropriate utilization of the sources [50,51]. Although efficient error-correction techniques have been adopted in QST, direct measurement of S maps automatically accounts for the detection errors and leads to more precise localization of maximal S values.

As an example, we demonstrate the application of S maps to benefit the QKD protocol by visualizing the state dependence of the optimal angle sets. First, the original E91 protocol focused on the EPR state, while S maps can be applied to any bipartite states to optimize the measurement settings. For the EPR state, the optimal angles are $\{\alpha_1, \alpha_3\} = \{0, 45^\circ\}$ and $\{\beta_1, \beta_3\} = \{22.5^\circ, 67.5^\circ\}$, which are mutually unbiased. However, with unbalanced states, the optimal angle sets can deviate from the settings above, as shown in Figs. S5 and S6 within the Supplemental Material [66]. Second, S maps not only optimize measurement settings but also indicate all the possible angle sets for secure QKD. The asymptotic key rate r in the limit of infinite key length under one-way classical postprocessing from Bob to Alice can be interpreted as the difference between Bob's and Eve's uncertainty about Alice's measurements, which must be positive to allow for effective QKD [76]. The key rate is determined by both the S values and the quantum bit error rates. By measuring S maps (and the concomitant r maps), one can obtain knowledge of what angle sets are usable for QKD for the given state, and the η_r value defined in Eq. (12) can help estimate the credibility of quantum cryptography. For an EPR state, the maximal $r = 1$, and the maximal $\eta_r \approx 0.16$. Our experimental η_r deviates from the maximal value mostly due to the nonzero ϕ_d . As the state approaches the EPR state, the η_r increases, indicating that more choices are available for secure QKD. In real-life applications, the measurement of S maps may be regarded as a calibration process of the system: once the states are prepared, Alice and Bob can measure their S map and determine the angle sets before the E91 protocol is performed, regardless of the existence of the eavesdropper Eve. Similarly, under the one-way (i.e., steering) scenario, other entanglement-based QKD protocols (such as the BBM92 protocol [77]) can be adapted using the S_{QS} maps [21].

Other than QKD, the S values acquired from the correlation maps warrant further applications. For example, S_{CHSH} values can be employed to quantify the fidelity of quantum teleportation. In quantum teleportation, the maximal violation of the CHSH inequality of a bipartite state is shown to lower bound its average fidelity for teleportation [31]. Moreover, S_{CHSH} values can be used in the certification of random number generation. The quantification of randomness may be described as a guessing process, where an observer, Eve, is trying to guess the outcome of Alice's measurement. Eve's strategy and the upper bound of the guessing probability are connected to S_{CHSH} . The relations between nonlocality and randomness also suggest a practical protocol for randomness generation in the device-independent scenario [33]. Lastly, S_{CHSH} values can also be used in the investigation of entanglement distillability. It is shown that entanglement distillability implies nonlocality [35, 78], and the violation of the CHSH inequality indicates that the state can be distilled [34]. All the applications above require the knowledge of the maximal S values, which can be acquired using the S map in a straightforward manner.

To conclude, we experimentally measure the S maps for nonlocality and steering. The S maps can be regarded as an experimental demonstration of the local polytope [9, 79]. As discussed in Appendix C, the full-domain maps demarcate the local polytope and can test the measured correlation for all Bell inequalities at the same time [80]. We apply S maps to various experimental bipartite states, including the EPR states, the unbalanced states, and the Werner states. As an application, we calibrate the QKD protocol with arbitrary bipartite states based on S maps. The S -map method potentially benefits the construction of QKD protocols with unknown sources, and the positive key ratio calculated from the S maps can help evaluate quantum communication security. Experimentally, S maps demonstrate significant benefits since they are more robust against systematic errors in the detection apparatus and involve minimal assumptions in the quantum model. This work warrants further investigation using loophole-free Bell's tests and multipartite states [17, 81]. Moreover, the S_{CHSH} maps are only necessary and sufficient to test nonlocality in the CHSH scenario, but the experimental method of correlation mapping can be extended to more generalized scenarios, for example, the I_{3322} scenario [79, 82] (more details can be found in Appendix C and Fig. S9 within the Supplemental Material [66]). Correlation maps are expected to have a variety of implications in quantum information applications.

ACKNOWLEDGMENTS

We would like to thank Professor P. Kwiat for stimulating discussions. This project has been made possible in part by Grant No. 2020–225832 from the

Chan Zuckerberg Initiative DAF, an advised fund of Silicon Valley Community Foundation, and National Institutes of Health Grants No. R35 CA220436 (Outstanding Investigator Award) and No. R01 EB028277.

APPENDIX A: DEFINITION OF QUANTUM STEERING

In the Hilbert spaces \mathcal{A} (for Alice) and \mathcal{B} (for Bob), we denote the eigenstates for the measurement axes $\hat{\alpha}$ and $\hat{\beta}$ as $A_\alpha \in \mathcal{A}$ and $B_\beta \in \mathcal{B}$ and denote the eigenvalues as a and b [9]. The LHV model assumes a hidden variable λ . For measurement outcomes a, b , the joint probability is

$$P_{\text{LHV}}(a, b|\alpha, \beta) = \int P(a|\alpha, \lambda)P(b|\beta, \lambda)p(\lambda)d\lambda, \quad (\text{A1})$$

where $P(a|\alpha, \lambda)$ and $P(b|\beta, \lambda)$ are the probabilities for Alice to obtain a and Bob to obtain b , respectively, with the indicated measurement axes. $p(\lambda)$ is the probability density function of λ .

The LHS model, as a subset of the LHV model, hypothesizes that Bob obtains a local hidden state ρ_λ related to λ . Hence, we substitute as follows:

$$P(b|\beta, \lambda) \rightarrow P_{\text{LHS}}(b|\beta, \rho_\lambda) = \text{Tr}(\Pi_{b|\beta}\rho_\lambda), \quad (\text{A2})$$

where $\Pi_{b|\beta}$ is the detection projector ($\Pi_{b|\beta} = |b\rangle_\beta\langle b|_\beta$). Therefore,

$$P_{\text{LHS}}(a, b|\alpha, \beta) = \int P(a|\alpha, \lambda)\text{Tr}(\Pi_{b|\beta}\rho_\lambda)p(\lambda)d\lambda. \quad (\text{A3})$$

The measurements by Alice with outcomes a lead to an unnormalized state $\rho_{a|\alpha}$ for Bob, given by

$$\rho_{a|\alpha}^{\text{LHS}} = \int P(a|\alpha, \lambda)p(\lambda)\rho_\lambda d\lambda. \quad (\text{A4})$$

Note that $\rho_{a|\alpha}^{\text{LHS}}$ is not “steered” by Alice because λ is “controlled” by the source. In contrast, quantum mechanics predicts

$$\rho_{a|\alpha}^{\text{QM}} = \text{Tr}_A[(\Pi_{a|\alpha} \otimes I_B)\rho_{AB}], \quad (\text{A5})$$

where I_B is the identity projector for Bob. If the following equation holds, a joint state ρ_{AB} is called unsteerable from Alice to Bob:

$$\rho_{a|\alpha}^{\text{QM}} = \rho_{a|\alpha}^{\text{LHS}}. \quad (\text{A6})$$

Otherwise, ρ_{AB} is called steerable [20, 83].

Below, we show two examples of two-level systems in pure states. First, a steerable entangled state along the \hat{z}

axis is chosen:

$$\rho_{AB} = \frac{|00\rangle + |11\rangle}{\sqrt{2}} \times \frac{\langle 00| + \langle 11|}{\sqrt{2}} = \frac{1}{2} (|00\rangle \langle 00| + |00\rangle \langle 11| + |11\rangle \langle 00| + |11\rangle \langle 11|). \quad (\text{A7})$$

In matrix form, we have

$$\rho_{AB} = \frac{1}{2} \begin{pmatrix} 1 & 0 & 0 & 1 \\ 0 & 0 & 0 & 0 \\ 0 & 0 & 0 & 0 \\ 1 & 0 & 0 & 1 \end{pmatrix}. \quad (\text{A8})$$

The projector of Alice to the eigenstate $|0\rangle_\alpha$ is

$$\begin{aligned} \Pi_{0|\alpha} &= |0\rangle_\alpha \langle 0|_\alpha = (\cos \alpha |0\rangle + \sin \alpha |1\rangle) (\cos \alpha \langle 0| + \sin \alpha \langle 1|) \\ &= \cos^2 \alpha |0\rangle \langle 0| + \cos \alpha \sin \alpha |0\rangle \langle 1| \\ &\quad + \cos \alpha \sin \alpha |1\rangle \langle 0| + \sin^2 \alpha |1\rangle \langle 1|, \end{aligned} \quad (\text{A9})$$

where α is the angle between the measurement axis $\hat{\alpha}$ and \hat{z} chosen by Alice. In matrix form, we have

$$\Pi_{0|\alpha} = \begin{pmatrix} \cos^2 \alpha & \cos \alpha \sin \alpha \\ \cos \alpha \sin \alpha & \sin^2 \alpha \end{pmatrix}. \quad (\text{A10})$$

For Bob, we have

$$I_B = \frac{1}{2} (|0\rangle \langle 0| + |1\rangle \langle 1|) = \frac{1}{2} \begin{pmatrix} 1 & 0 \\ 0 & 1 \end{pmatrix}. \quad (\text{A11})$$

We first compute $\rho_{a|\alpha}^{\text{QM}}$ as follows:

$$\Pi_{0|\hat{\alpha}} \otimes I_B = \frac{1}{2} \begin{pmatrix} \cos^2 \alpha & 0 & \cos \alpha \sin \alpha & 0 \\ 0 & \cos^2 \alpha & 0 & \cos \alpha \sin \alpha \\ \cos \alpha \sin \alpha & 0 & \sin^2 \alpha & 0 \\ 0 & \cos \alpha \sin \alpha & 0 & \sin^2 \alpha \end{pmatrix}, \quad (\text{A12})$$

$$(\Pi_{0|\hat{\alpha}} \otimes I_B) \rho_{AB} = \frac{1}{2} \begin{pmatrix} \cos^2 \alpha & 0 & 0 & \cos^2 \alpha \\ \cos \alpha \sin \alpha & 0 & 0 & \cos \alpha \sin \alpha \\ \cos \alpha \sin \alpha & 0 & 0 & \cos \alpha \sin \alpha \\ \sin^2 \alpha & 0 & 0 & \sin^2 \alpha \end{pmatrix}, \quad (\text{A13})$$

$$\begin{aligned} \rho_{a|\alpha}^{\text{QM}} &= \text{Tr}_A[(\Pi_{0|\hat{\alpha}} \otimes I_B) \rho_{AB}] \\ &= \frac{1}{2} \begin{pmatrix} \cos^2 \alpha & \cos \alpha \sin \alpha \\ \cos \alpha \sin \alpha & \sin^2 \alpha \end{pmatrix}. \end{aligned} \quad (\text{A14})$$

Note the outcome equals $(1/2)|0\rangle_\alpha \langle 0|_\alpha$. We then compute $\rho_{a|\alpha}^{\text{LHS}}$. The hidden state can be written as

$$\rho_\lambda = (C_0|0\rangle + C_1|1\rangle) (C_0^* \langle 0| + C_1^* \langle 1|), \quad (\text{A15})$$

whose matrix form is

$$\rho_\lambda = \begin{pmatrix} |C_0|^2 & C_0^* C_1 \\ C_1^* C_0 & |C_1|^2 \end{pmatrix}. \quad (\text{A16})$$

We assume that the average of the probability $P(0|\alpha, \lambda)$ over the hidden variable λ matches the prediction by

quantum mechanics:

$$\begin{aligned} \int d\lambda P(0|\alpha, \lambda) p(\lambda) &= \left(\langle 0|_\alpha \left[\frac{1}{\sqrt{2}}(|0\rangle + |1\rangle) \right] \right)^2 \\ &= \frac{1}{2}(1 + \sin 2\alpha). \end{aligned} \quad (\text{A17})$$

If Equation (A6) holds, we have

$$\begin{aligned} \rho_{a|\alpha}^{\text{LHS}} &= \int d\lambda P(0|\alpha, \lambda) p(\lambda) \begin{pmatrix} |C_0|^2 & C_0^* C_1 \\ C_1^* C_0 & |C_1|^2 \end{pmatrix} \\ &= \frac{1}{2} \begin{pmatrix} \cos^2 \alpha & \cos \alpha \sin \alpha \\ \cos \alpha \sin \alpha & \sin^2 \alpha \end{pmatrix}. \end{aligned} \quad (\text{A18})$$

Let us prove that there does not exist a $p(\lambda)\rho_\lambda$ to satisfy Eq. (A18). The diagonal terms of Eq. (A18) gives

$$\int d\lambda P(0|\hat{\alpha}, \lambda) p(\lambda) |C_0|^2 = \frac{1}{2} \cos^2 \alpha, \quad (\text{A19})$$

$$\int d\lambda P(0|\hat{\alpha}, \lambda) p(\lambda) |C_1|^2 = \frac{1}{2} \sin^2 \alpha. \quad (\text{A20})$$

Merging Eqs. (A19) and (A20) produces

$$\int d\lambda P(0|\hat{\alpha}, \lambda)p(\lambda)(|C_0|^2 + |C_1|^2) = \frac{1}{2}. \quad (\text{A21})$$

Using $|C_0|^2 + |C_1|^2 = 1$ and substituting Eq. (A17) into Eq. (A21), we find

$$\frac{1}{2}(1 + \sin 2\alpha) = \frac{1}{2}. \quad (\text{A22})$$

This equation yields $\alpha = 0^\circ$ or 90° , which contradicts the fact that α can be set to any angle. Therefore, a system with the joint state ρ_{AB} given by Eq. (A7) is steerable from Alice to Bob.

Second, an unsteerable product state along the \hat{z} axis is chosen:

$$\rho_{AB} = |00\rangle\langle 00|. \quad (\text{A23})$$

In matrix form, we have

$$\rho_{AB} = \begin{pmatrix} 1 & 0 & 0 & 0 \\ 0 & 0 & 0 & 0 \\ 0 & 0 & 0 & 0 \\ 0 & 0 & 0 & 0 \end{pmatrix}. \quad (\text{A24})$$

Similar to the example (1), we first compute $\rho_{a|\alpha}^{\text{QM}}$ as follows:

$$\Pi_{0|\hat{\alpha}} \otimes I_B = \begin{pmatrix} \cos^2\alpha & 0 & \cos\alpha \sin\alpha & 0 \\ 0 & \cos^2\alpha & 0 & \cos\alpha \sin\alpha \\ \cos\alpha \sin\alpha & 0 & \sin^2\alpha & 0 \\ 0 & \cos\alpha \sin\alpha & 0 & \sin^2\alpha \end{pmatrix}, \quad (\text{A25})$$

$$(\Pi_{0|\hat{\alpha}} \otimes I_B)\rho_{AB} = \begin{pmatrix} \cos^2\alpha & 0 & 0 & 0 \\ 0 & 0 & 0 & 0 \\ \cos\alpha \sin\alpha & 0 & 0 & 0 \\ 0 & 0 & 0 & 0 \end{pmatrix}, \quad (\text{A26})$$

$$\rho_{a|\alpha}^{\text{QM}} = \text{Tr}_A[(\Pi_{0|\hat{\alpha}} \otimes I_B)\rho_{AB}] = \begin{pmatrix} \cos^2\alpha & 0 \\ 0 & 0 \end{pmatrix}. \quad (\text{A27})$$

We then compute $\rho_{a|\alpha}^{\text{LHS}}$. The hidden state can be written as

$$\rho_\lambda = (C_0|0\rangle + C_1|1\rangle)(C_0^*\langle 0| + C_1^*\langle 1|), \quad (\text{A28})$$

whose expansion yields

$$\rho_\lambda = \begin{pmatrix} |C_0|^2 & C_0^*C_1 \\ C_1^*C_0 & |C_1|^2 \end{pmatrix}, \quad (\text{A29})$$

where $|C_0|^2 + |C_1|^2 = 1$. We assume that the average of the probability $P(0|\alpha, \lambda)$ over the hidden variable λ matches the prediction by quantum mechanics.

$$\int d\lambda P(0|\alpha, \lambda)p(\lambda) = (\langle 0|_\alpha|0\rangle)^2 = \cos^2\alpha. \quad (\text{A30})$$

Therefore, we have

$$\rho_{a|\alpha}^{\text{LHS}} = \int d\lambda P(0|\alpha, \lambda)p(\lambda) \begin{pmatrix} |C_0|^2 & C_0^*C_1 \\ C_1^*C_0 & |C_1|^2 \end{pmatrix}. \quad (\text{A31})$$

Let $|C_0| = 1, C_1 = 0$, we reach

$$\rho_{a|\alpha}^{\text{LHS}} = \cos^2\alpha \begin{pmatrix} 1 & 0 \\ 0 & 0 \end{pmatrix} = \begin{pmatrix} \cos^2\alpha & 0 \\ 0 & 0 \end{pmatrix}. \quad (\text{A32})$$

Therefore, Eq. (A6) holds, proving that a system with the joint state ρ_{AB} given by Eq. (A23) is unsteerable from Alice to Bob.

APPENDIX B: EXPERIMENTAL METHODS

System construction and calibration

In our system [Fig. 1(b)], we use a 50-mW, 405-nm continuous-wave laser (GPD405-50, Power Technology Inc.) to generate pump light. For signal and idler photon generation, we use one set of paired BBO crystals [$5 \times 5 \times 0.5 \text{ mm}^3$ each, PABBO5050-405(I)-HA3, Newlight Photonics Inc.]. The two crystals are cut for type-I SPDC pumped by 405 nm with a half opening angle of 3° and are mounted back to back with one crystal rotated

by 90° about the normal axis to the incidence face. The polarization angle of the pump light is controlled by a Glan-Laser polarizer (GL10-A, Thorlabs Inc.) and a half-wave plate (WPA03-H-405, Newlight Photonics Inc.). The phase of the pump light is adjusted by a variable wave plate (5540, Newport) and a quartz plate (QAT25100-A, Newlight Photonics Inc.). For polarization selection, two half-wave plates (WPA03-H-810, Newlight Photonics Inc.) at 810 nm are mounted on two motorized precision rotation mounts (PRM1Z8, Thorlabs Inc.) followed by two polarizing beam splitters (PBS201, Thorlabs Inc.). For single-photon detection, we use two single-photon counting modules (SPCM-AQRH-16, Excelitas Technologies) with a dark count rate of less than 25 Hz. The two SPCMs are connected to a time controller (ID900-TCSPC-HR, ID Quantique) with a 13-ps digital time resolution for coincidence counting. The motorized rotation mounts, the SPCMs, and the time controller are integrated into a custom-written LabVIEW program for automated measurements. The setup is placed in a dedicated light-shielding box, and the SPCMs are equipped with the necessary bandpass and highpass filters to minimize ambient light contamination.

An additional 100-mW, 635-nm continuous-wave laser (MLL-III-635-100 mW, Changchun New Industries Optoelectronics Technology Co., Ltd.) is used as guidance light to assist alignment. Prior to formal measurements, we perform two finer scans on α and β from 0° to 180° with a step size of 1° and record the raw count in each SPCM. We then fit each curve to a squared cosine function to find the minimum (or maximum). The deviation of the minimum (or maximum) from 90° is recorded as the mounting error of the two HWPs. All the consequent measurements are then shifted by these values to compensate for the errors.

S_{CHSH} calculation in Bell's test

For each round of Bell's test, we rotate α from 0° to 135° with a step size of 45° . For each fixed α , we rotate β from 22.5° to 157.5° with a step size of 45° . Although only 16 projective measurements are needed to calculate the S_{CHSH} value, we measure 36 points to visualize the variation of the coincidences better. After recording the coincidence counts $N(H, H|\alpha, \beta)$ at each step with an acquisition time of 1 s and a coincidence detection window of 8 ns, we calculate the correlation value based on the modified Eq. (2) as

$$E(\alpha, \beta) = \frac{N(H, H|\alpha, \beta) + N(H, H|\alpha + 90^\circ, \beta + 90^\circ) - N(H, H|\alpha + 90^\circ, \beta) - N(H, H|\alpha, \beta + 90^\circ)}{N(H, H|\alpha, \beta) + N(H, H|\alpha + 90^\circ, \beta + 90^\circ) + N(H, H|\alpha + 90^\circ, \beta) + N(H, H|\alpha, \beta + 90^\circ)}. \quad (\text{B1})$$

The S_{CHSH} value is then evaluated according to Eq. (3). Note S2 within the Supplemental Material shows more details of the fitted curves in Fig. 2(c) [66].

Full-domain coincidence and correlation measurement

Prior to the full-domain coincidence measurement with different degrees of bipartite ellipticities, we first perform a 36-point scanning as described above and fit the results to Eq. (B1) to calculate θ_p and ϕ_d . We then tune the half-wave plate, the variable wave plate, and the quartz plate and repeat the scanning until we reach the desired θ_p and ϕ_d . We then fix the setup and scan the angles α and β both from 0° to 180° with a step size of 3° and record the coincidences within 1 s at each point. The scanning renders a two-dimensional coincidence map $N(H, H|\alpha, \beta; \theta_p, \phi_d)$. More details of the fitting can be found in Note S2 within the Supplemental Material [66].

To get the correlation map (E map), we shift the coincidence map $N(H, H)$ by 90° along the α axis [to acquire $N(V, H)$ map], the β axis [to acquire $N(H, V)$ map], and the diagonal axis [to acquire $N(V, V)$ map]. Afterwards, we construct the four maps according to Eq. (2) to acquire the

correlation map, as illustrated in Fig. S2 within the Supplemental Material [66]. The E map can then be used to calculate the S_{CHSH} map and S_{QS} map according to Eqs. (3) and (5), respectively.

Quantum key rate calculation

Assuming a 100% detector efficiency and an infinitely long quantum key, the rate of effective (successful) key is given by [22]

$$r = 1 - h\left(\frac{1 + \sqrt{(S_{\text{CHSH}}/2)^2 - 1}}{2}\right) - h(\epsilon), \quad (\text{B2})$$

where $h(x) = -x\log_2 x - (1-x)\log_2(1-x)$ is the binary entropy function, and $\epsilon = P(a_i \neq b_j | \alpha_i = \beta_j)$ is the quantum bit error rate.

APPENDIX C: CONNECTION BETWEEN THE CORRELATION MAP AND THE LOCAL POLYTOPE

Consider two parties, Alice and Bob, performing measurements on a shared physical system. Each observer has

a choice of m different measurements to perform on their system. Each measurement can yield Δ possible outcomes. We focus on the CHSH scenario, where $m = 2, \Delta = 2$. Following the notation in the main text, let $P(a, b|\alpha, \beta)$ denote the joint probability to obtain the output pair (a, b) given the input pair (α, β) under the CHSH scenario. A Bell scenario is then completely characterized by $\Delta^2 m^2$ such joint probabilities, one for each possible pair of inputs and outputs [9]. We refer to the set $\mathbf{P} = \{P(a, b|\alpha, \beta)\}$ of all these probabilities as a behavior [84].

In the LHV model as described by Eq. (1), there are only a finite number of hidden variables λ_i , each of which defines an assignment of one of the possible outputs to each input [9]. Let λ_i define an assignment of outputs a_α and b_β for each of the inputs α and β , the resulting deterministic behavior is denoted as \mathbf{D}_i . All Δ^{2m} deterministic points $\{\mathbf{D}_i\}$ form the local polytope [9]. A behavior \mathbf{P} is local if and only if it can be written as a convex combination of these deterministic points [80]. The linear program can be written as

$$\max v, \text{ such that } v\mathbf{P} + (1 - v)\mathbf{W} = \sum_i c_i \mathbf{D}_i, \quad (\text{C1})$$

where \mathbf{W} denotes the behavior of the white noise, $c_i > 0, \sum_i c_i = 1$. When the optimal $v < 1$, \mathbf{P} is nonlocal.

Equation (C1) and its dual form not only indicate the method to test whether \mathbf{P} is nonlocal, but also provide a procedure for finding, for any \mathbf{P} , a Bell inequality that detects its nonlocality [9]. The correlation map can therefore be regarded as an experimental measurement of the full-domain behaviors, which can be used to test for all Bell inequalities at the same time.

Moreover, the full-domain correlation maps can be extended to other scenarios where multiple measurement settings or outcomes are involved, different inequalities are needed to characterize the local polytope, and the S maps warrant modification accordingly. For example, when $m = 3, \Delta = 2$, the local polytope is not only defined by the CHSH inequality but also the I_{3322} inequality [79,85]. In this scenario, a six-dimensional S_{3322} map is needed, which can be naturally extended from the CHSH-based 4D maps. A 3D cross section of the S_{3322} map is shown in Fig. S9 within the Supplemental Material [66].

Leuchs, Colloquium: The Einstein-Podolsky-Rosen paradox: From concepts to applications, *Rev. Mod. Phys.* **81**, 1727 (2009).

- [4] R. Horodecki, P. Horodecki, M. Horodecki, and K. Horodecki, Quantum entanglement, *Rev. Mod. Phys.* **81**, 865 (2009).
- [5] J. S. Bell, On the Einstein Podolsky Rosen paradox, *Physics Physique Fizika* **1**, 195 (1964).
- [6] C. H. Bennett, G. Brassard, C. Crépeau, R. Jozsa, A. Peres, and W. K. Wootters, Teleporting an Unknown Quantum State via Dual Classical and Einstein-Podolsky-Rosen Channels, *Phys. Rev. Lett.* **70**, 1895 (1993).
- [7] A. K. Ekert, Quantum Cryptography Based on Bell's Theorem, *Phys. Rev. Lett.* **67**, 661 (1991).
- [8] M. Hillery, V. Bužek, and A. Berthiaume, Quantum secret sharing, *Phys. Rev. A* **59**, 1829 (1999).
- [9] N. Brunner, D. Cavalcanti, S. Pironio, V. Scarani, and S. Wehner, Bell nonlocality, *Rev. Mod. Phys.* **86**, 419 (2014).
- [10] M. Zych, F. Costa, I. Pikovski, and Č. Brukner, Bell's theorem for temporal order, *Nat. Commun.* **10**, 1 (2019).
- [11] R. F. Werner, Quantum states with Einstein-Podolsky-Rosen correlations admitting a hidden-variable model, *Phys. Rev. A* **40**, 4277 (1989).
- [12] J. F. Clauser, M. A. Horne, A. Shimony, and R. A. Holt, Proposed Experiment to Test Local Hidden-Variable Theories, *Phys. Rev. Lett.* **23**, 880 (1969).
- [13] E. Schrödinger, Discussion of probability relations between separated systems, *Math. Proc. Camb. Philos. Soc.* **31**, 555 (1935).
- [14] H. M. Wiseman, S. J. Jones, and A. C. Doherty, Steering, Entanglement, Nonlocality, and the Einstein-Podolsky-Rosen Paradox, *Phys. Rev. Lett.* **98**, 140402 (2007).
- [15] D. J. Saunders, S. J. Jones, H. M. Wiseman, and G. J. Pryde, Experimental EPR-steering using Bell-local states, *Nat. Phys.* **6**, 11 (2010).
- [16] V. Händchen, T. Eberle, S. Steinlechner, A. Samblowski, T. Franz, R. F. Werner, and R. Schnabel, Observation of one-way Einstein-Podolsky-Rosen steering, *Nat. Photonics* **6**, 9 (2012).
- [17] B. Wittmann, S. Ramelow, F. Steinlechner, N. K. Langford, N. Brunner, H. M. Wiseman, R. Ursin, and A. Zeilinger, Loophole-free Einstein-Podolsky-Rosen experiment via quantum steering, *New J. Phys.* **14**, 053030 (2012).
- [18] D. Cavalcanti and P. Skrzypczyk, Quantum steering: A review with focus on semidefinite programming, *Rep. Prog. Phys.* **80**, 024001 (2016).
- [19] P. Kunkel, M. Präfer, H. Strobel, D. Linnemann, A. Frölian, T. Gasenzer, M. Gärttner, and M. K. Oberthaler, Spatially distributed multipartite entanglement enables EPR steering of atomic clouds, *Science* **360**, 413 (2018).
- [20] R. Uola, A. C. S. Costa, H. C. Nguyen, and O. Gühne, Quantum steering, *Rev. Mod. Phys.* **92**, 015001 (2020).
- [21] C. Branciard, E. G. Cavalcanti, S. P. Walborn, V. Scarani, and H. M. Wiseman, One-sided device-independent quantum key distribution: Security, feasibility, and the connection with steering, *Phys. Rev. A* **85**, 010301 (2012).
- [22] A. Acín, N. Brunner, N. Gisin, S. Massar, S. Pironio, and V. Scarani, Device-Independent Security of Quantum Cryptography against Collective Attacks, *Phys. Rev. Lett.* **98**, 230501 (2007).

- [23] M. Curty, M. Lewenstein, and N. Lütkenhaus, Entanglement as a Precondition for Secure Quantum Key Distribution, *Phys. Rev. Lett.* **92**, 217903 (2004).
- [24] J. Barrett, L. Hardy, and A. Kent, No Signaling and Quantum Key Distribution, *Phys. Rev. Lett.* **95**, 010503 (2005).
- [25] E. G. Cavalcanti, C. J. Foster, M. Fuwa, and H. M. Wiseman, Analog of the Clauser–Horne–Shimony–Holt inequality for steering, *J. Opt. Soc. Am. B* **32**, A74 (2015).
- [26] D. Dehlinger and M. W. Mitchell, Entangled photons, non-locality, and Bell inequalities in the undergraduate laboratory, *Am. J. Phys.* **70**, 903 (2002).
- [27] A. Peres, All the Bell inequalities, *Found. Phys.* **29**, 589 (1999).
- [28] J. F. Clauser and A. Shimony, Bell’s theorem. Experimental tests and implications, *Rep. Prog. Phys.* **41**, 1881 (1978).
- [29] A. Aspect, P. Grangier, and G. Roger, Experimental Tests of Realistic Local Theories via Bell’s Theorem, *Phys. Rev. Lett.* **47**, 460 (1981).
- [30] W. Tittel, J. Brendel, H. Zbinden, and N. Gisin, Violation of Bell Inequalities by Photons More Than 10 Km Apart, *Phys. Rev. Lett.* **81**, 3563 (1998).
- [31] R. Horodecki, M. Horodecki, and P. Horodecki, Teleportation, Bell’s inequalities and inseparability, *Phys. Lett. A* **222**, 21 (1996).
- [32] D. Cavalcanti, A. Acín, N. Brunner, and T. Vértesi, All quantum states useful for teleportation are nonlocal resources, *Phys. Rev. A* **87**, 042104 (2013).
- [33] S. Pironio, A. Acín, S. Massar, A. Boyer de la Giroday, D. N. Matsukevich, P. Maunz, S. Olmschenk, D. Hayes, L. Luo, T. A. Manning, *et al.*, Random numbers certified by Bell’s theorem, *Nature* **464**, 7291 (2010).
- [34] A. Acín, Distillability, Bell Inequalities, and Multiparticle Bound Entanglement, *Phys. Rev. Lett.* **88**, 027901 (2001).
- [35] L. Masanes, Asymptotic Violation of Bell Inequalities and Distillability, *Phys. Rev. Lett.* **97**, 050503 (2006).
- [36] N. Gisin, G. Ribordy, W. Tittel, and H. Zbinden, Quantum cryptography, *Rev. Mod. Phys.* **74**, 145 (2002).
- [37] R. Arnon-Friedman, F. Dupuis, O. Fawzi, R. Renner, and T. Vidick, Practical device-independent quantum cryptography via entropy accumulation, *Nat. Commun.* **9**, 1 (2018).
- [38] F. Dupuis, O. Fawzi, and R. Renner, Entropy accumulation, *Commun. Math. Phys.* **379**, 867 (2020).
- [39] D. P. Nadlinger, P. Drmota, B. C. Nichol, G. Araneda, D. Main, R. Srinivas, D. M. Lucas, C. J. Ballance, K. Ivanov, E. Y.-Z. Tan, *et al.*, Experimental quantum key distribution certified by Bell’s theorem, *Nature* **607**, 7920 (2022).
- [40] P. Skrzypczyk, M. Navascués, and D. Cavalcanti, Quantifying Einstein–Podolsky–Rosen Steering, *Phys. Rev. Lett.* **112**, 180404 (2014).
- [41] W.-Y. Sun, D. Wang, J.-D. Shi, and L. Ye, Exploration quantum steering, nonlocality and entanglement of two-qubit x-state in structured reservoirs, *Sci. Rep.* **7**, 1 (2017).
- [42] Q. Quan, H. Zhu, H. Fan, and W.-L. Yang, Einstein–Podolsky–Rosen correlations and bell correlations in the simplest scenario, *Phys. Rev. A* **95**, 062111 (2017).
- [43] S. L. Braunstein and C. M. Caves, Wringing out better Bell inequalities, *Ann. Phys.* **202**, 22 (1990).
- [44] M. A. Rowe, D. Kielpinski, V. Meyer, C. A. Sackett, W. M. Itano, C. Monroe, and D. J. Wineland, Experimental violation of a Bell’s inequality with efficient detection, *Nature* **409**, 6822 (2001).
- [45] M. Giustina, A. Mech, S. Ramelow, B. Wittmann, J. Kofler, J. Beyer, A. Lita, B. Calkins, T. Gerrits, S. W. Nam, *et al.*, Bell violation using entangled photons without the fair-sampling assumption, *Nature* **497**, 7448 (2013).
- [46] K. Vogel and H. Risken, Determination of quasiprobability distributions in terms of probability distributions for the rotated quadrature phase, *Phys. Rev. A* **40**, 2847 (1989).
- [47] D. F. James, P. G. Kwiat, W. J. Munro, and A. G. White, Measurement of qubits, *Phys. Rev. A* **64**, 052312 (2001).
- [48] M. Paris and J. Rehacek, *Quantum State Estimation* (Springer Science & Business Media, Germany, 2004).
- [49] H. Häffner, W. Hänsel, C. F. Roos, J. Benhelm, D. Chekalakar, M. Chwalla, T. Körber, U. D. Rapol, M. Riebe, P. O. Schmidt, *et al.*, Scalable multiparticle entanglement of trapped ions, *Nature* **438**, 7068 (2005).
- [50] A. Acín, N. Gisin, and L. Masanes, From Bell’s Theorem to Secure Quantum Key Distribution, *Phys. Rev. Lett.* **97**, 120405 (2006).
- [51] L. Lydersen, C. Wiechers, C. Wittmann, D. Elser, J. Skaar, and V. Makarov, Hacking commercial quantum cryptography systems by tailored bright illumination, *Nature Photon* **4**, 10 (2010).
- [52] C. Schwemmer, L. Knips, D. Richart, H. Weinfurter, T. Moroder, M. Kleinmann, and O. Gühne, Systematic Errors in Current Quantum State Tomography Tools, *Phys. Rev. Lett.* **114**, 080403 (2015).
- [53] D. Gross, Y.-K. Liu, S. T. Flammia, S. Becker, and J. Eisert, Quantum State Tomography via Compressed Sensing, *Phys. Rev. Lett.* **105**, 150401 (2010).
- [54] D. Rosset, R. Ferretti-Schöbitz, J.-D. Bancal, N. Gisin, and Y.-C. Liang, Imperfect measurement settings: implications for quantum state tomography and entanglement witnesses, *Phys. Rev. A* **86**, 062325 (2012).
- [55] T. Moroder, M. Kleinmann, P. Schindler, T. Monz, O. Gühne, and R. Blatt, Certifying Systematic Errors in Quantum Experiments, *Phys. Rev. Lett.* **110**, 180401 (2013).
- [56] G. Torlai, G. Mazzola, J. Carrasquilla, M. Troyer, R. Melko, and G. Carleo, Neural-network quantum state tomography, *Nature Phys.* **14**, 5 (2018).
- [57] H. Di Lorenzo Pires, F. M. G. J. Coppens, and M. P. van Exter, Type-I spontaneous parametric down-conversion with a strongly focused pump, *Phys. Rev. A* **83**, 033837 (2011).
- [58] M. Kaur and M. Singh, Quantum double-double-slit experiment with momentum entangled photons, *Sci. Rep.* **10**, 1 (2020).
- [59] P. G. Kwiat, K. Mattle, H. Weinfurter, A. Zeilinger, A. V. Sergienko, and Y. Shih, New High-Intensity Source of Polarization-Entangled Photon Pairs, *Phys. Rev. Lett.* **75**, 4337 (1995).
- [60] B.-S. Shi and A. Tomita, Generation of a pulsed polarization entangled photon pair using a Sagnac interferometer, *Phys. Rev. A* **69**, 013803 (2004).
- [61] S. Karan, S. Aarav, H. Bharadhwaj, L. Taneja, A. De, G. Kulkarni, N. Meher, and A. K. Jha, Phase matching in

- β -barium borate crystals for spontaneous parametric down-conversion, *J. Opt.* **22**, 083501 (2020).
- [62] B. S. Cirel'son, Quantum generalizations of Bell's inequality, *Lett. Math. Phys.* **4**, 93 (1980).
- [63] J. Shang, Z. Zhang, and H. K. Ng, Superfast maximum-likelihood reconstruction for quantum tomography, *Phys. Rev. A* **95**, 062336 (2017).
- [64] W. K. Wootters, Entanglement of Formation of an Arbitrary State of Two Qubits, *Phys. Rev. Lett.* **80**, 2245 (1998).
- [65] A. G. White, D. F. V. James, P. H. Eberhard, and P. G. Kwiat, Nonmaximally Entangled States: Production, Characterization, and Utilization, *Phys. Rev. Lett.* **83**, 3103 (1999).
- [66] See Supplemental Material at <http://link.aps.org/supplemental/10.1103/PhysRevApplied.19.034049> for fitting equations and additional experimental and simulated results.
- [67] D. Fan, W. Guo, and L. Wei, Experimentally testing the Bell inequality violation by optimizing the measurement settings, *J. Opt. Soc. Am. B* **29**, 3429 (2012).
- [68] C. A. Fuchs, N. Gisin, R. B. Griffiths, C.-S. Niu, and A. Peres, Optimal eavesdropping in quantum cryptography. I. Information bound and optimal strategy, *Phys. Rev. A* **56**, 1163 (1997).
- [69] C. H. Bennett, G. Brassard, C. Crepeau, and U. M. Maurer, Generalized privacy amplification, *IEEE Trans. Inform. Theory* **41**, 1915 (1995).
- [70] S. Pironio, A. Acín, N. Brunner, N. Gisin, S. Massar, and V. Scarani, Device-independent quantum key distribution secure against collective attacks, *New J. Phys.* **11**, 045021 (2009).
- [71] S. J. Jones, H. M. Wiseman, and A. C. Doherty, Entanglement, Einstein-Podolsky-Rosen correlations, Bell nonlocality, and steering, *Phys. Rev. A* **76**, 052116 (2007).
- [72] M. T. Quintino, T. Vértesi, D. Cavalcanti, R. Augusiak, M. Demianowicz, A. Acín, and N. Brunner, Inequivalence of entanglement, steering, and Bell nonlocality for general measurements, *Phys. Rev. A* **92**, 032107 (2015).
- [73] M. A. Nielsen and I. L. Chuang, Quantum Computation and Quantum Information: 10th Anniversary Edition,
- [74] W. K. Wootters and B. D. Fields, Optimal state-determination by mutually unbiased measurements, *Ann. Phys.* **191**, 363 (1989).
- [75] D. Gottesman, H.-K. Lo, N. Lutkenhaus, and J. Preskill, in *International Symposium OnInformation Theory, 2004. ISIT 2004. Proceedings* (2004), p. 136.
- [76] I. Devetak and A. Winter, Distillation of secret key and entanglement from quantum states, *Proc. R. Soc. A: Math. Phys. Eng. Sci.* **461**, 207 (2005).
- [77] C. H. Bennett, G. Brassard, and N. D. Mermin, Quantum Cryptography without Bell's Theorem, *Phys. Rev. Lett.* **68**, 557 (1992).
- [78] T. Vértesi and N. Brunner, Disproving the Peres conjecture by showing Bell nonlocality from bound entanglement, *Nat. Commun.* **5**, 1 (2014).
- [79] M. Froissart, Constructive generalization of Bell's inequalities, *Il Nuovo Cimento B* **64**, 241 (1981).
- [80] D. Kaszlikowski, P. Gnaciński, M. Żukowski, W. Miklaszewski, and A. Zeilinger, Violations of Local Realism by Two Entangled N-Dimensional Systems Are Stronger than for Two Qubits, *Phys. Rev. Lett.* **85**, 4418 (2000).
- [81] J. Barrett, D. Collins, L. Hardy, A. Kent, and S. Popescu, Quantum nonlocality, bell inequalities, and the memory loophole, *Phys. Rev. A* **66**, 042111 (2002).
- [82] D. Collins and N. Gisin, A relevant two qubit bell inequality inequivalent to the CHSH inequality, *J. Phys. A: Math. Gen.* **37**, 1775 (2004).
- [83] D. Cavalcanti, L. Guerini, R. Rabelo, and P. Skrzypczyk, General Method for Constructing Local Hidden Variable Models for Entangled Quantum States, *Phys. Rev. Lett.* **117**, 190401 (2016).
- [84] B. S. Tsirelson, Some results and problems on quantum Bell-type inequalities, *Hadronic J. Suppl.* **8**, 329 (1993).
- [85] F. Bernards and O. Gühne, Generalizing Optimal Bell Inequalities, *Phys. Rev. Lett.* **125**, 200401 (2020).